Physics of Fluids

Wing-tip vortex dynamics at moderate Reynolds numbers

Cite as: Phys. Fluids **33**, 035111 (2021); https://doi.org/10.1063/5.0039492
Submitted: 03 December 2020 • Accepted: 26 January 2021 • Published Online: 04 March 2021

T. A. Smith and Y. Ventikos

Physics of Fluids ARTICLE scitation.org/journal/phf

Wing-tip vortex dynamics at moderate Reynolds numbers

Cite as: Phys. Fluids **33**, 035111 (2021); doi: 10.1063/5.0039492
Submitted: 3 December 2020 · Accepted: 26 January 2021 ·
Published Online: Pls check Date

T. A. Smith[a] and Y. Ventikos

AFFILIATIONS

Department of Mechanical Engineering, University College London, London WC1E 7JE, United Kingdom

[a]Author to whom correspondence should be addressed: tom.smith.17@ucl.ac.uk

ABSTRACT

The flow over a flat-tipped wing at three Reynolds numbers: $Re = 1 \times 10^4$, $Re = 4 \times 10^4$, and $Re = 1 \times 10^5$ is investigated using direct numerical simulation. A set of grid independent results are obtained which allow for the dynamics of the tip flow, trailing vortices, and their interplay with the boundary layer dynamics to be examined in detail. The results show significant changes across the Reynolds number range. At the lowest Reynolds number, a single trailing vortex forms downstream of the trailing edge, whereas multiple vortices form over the tip at higher Reynolds numbers. The tip geometry is shown to be important with regard to the development of different structures and in the transition of the flow from laminar to turbulent. This is due to unstable shear layers, with turbulent flow becoming entrained in the vortex cores at higher Reynolds numbers. These changing vortex dynamics mean that the value of the minimum vortex core pressure and its location change with Reynolds number. This has important consequences for cavitation inception and scaling for hydrodynamic applications. The influence of the tip flow on the boundary layer is further considered by comparing the flow with that of an infinite-span wing. Analysis of the two cases shows that the tip flow reduces the effective angle of attack, which prevents the flow separation at the leading edge that is responsible for the boundary layer transition for the infinite-span case. This, in turn, changes the character of the trailing edge flow which would have significant consequences on the trailing edge noise.

I. INTRODUCTION

Tip vortices have long been of interest in the fluid dynamics community due to their importance in a wide-range of applications. When present, they can have a number of undesirable effects including a reduction in the lift-drag ratio of lifting surfaces as well and producing noise and causing vibration.

Despite many decades of research into the roll-up process as well as the near and far-field dynamics, many questions remain unanswered. The inherent three-dimensionality of the flow and the complex dynamics of the roll-up process, shear layer instabilities, and the role of the boundary layer make the study of tip vortices challenging both experimentally and numerically. Many experimental works have investigated the formation of wing-tip vortices.[1–3] These studies show that multiple vortices can form over the tip depending on both the geometry and operating conditions. Giuni and Green[3] showed that the resulting trailing vortex is strongly affected by the interacting structures that form over the tip, highlighting the importance of accurately modeling the roll-up process if one wishes to better understand the near-wake and far-wake dynamics.

There has been much attention given to the far-wake of tip vortex flows, as the persistence of wing-tip vortices is of importance to aircraft and runway operations and Spalart[4] provides an excellent review of much of the earlier work in this field. Subsequent studies have added to our overall understanding of vortex stability and meandering.[5–7]

The problems posed by wing-tip vortices have naturally led to extensive research into their modification and suppression. Much of early work focused on modifications to the tip geometry,[8] and the addition of winglets, as well as blowing and/or suction. Not all such modifications have proved successful, as highlighted by Dunham.[9] More recent studies consider both passive and active measures to reduce the strength and persistence of tip vortices. Passive techniques are considered by Lee and Su,[10] Lee and Choi,[11] who show experimentally that a reverse half-delta wing mounted to the tip of a NACA0012 foil resulted in a weaker tip vortex being produced. Active techniques such as the use of flaps have also been considered.[12,13] Such techniques are not always successful and it appears that a more detailed understanding of the vortex roll-up process and near-field dynamics is needed to make consistent improvements across a broader range of operating conditions.

More limited progress has been made in suppressing tip vortices produced by marine propeller blades. Tip vortices have been shown to be important acoustic sources for marine propellers.[14–16] In their study of propeller noise, Ianniello *et al.*[15] showed that the tip vortex was the dominant source of non-cavitating noise in the far-field. Tip vortices also play an important role in cavitation, as tip vortex cavitation is often the first to appear on a modern marine propeller[17] and a great deal of effort has gone into the prediction of tip-vortex cavitation inception. The vast majority of this work, be it experimental or numerical, has been conducted at model scale, with scaling laws being used to determine the full-scale tip vortex dynamics which help us to determine the point of cavitation inception. These scaling laws are often based on early work of McCormick,[18] who suggested that the vortex core size is a linear function of the thickness of the boundary layer. This gave rise to a power law for scaling and a number of variations have been proposed.[19] These scaling laws are based on severe simplifications of the underlying flow and, as a result, require extensive tuning based on experimental data sets. A more complete description of the physics of the vortex roll-up process over the tip should allow for improvements to such scaling laws to be made.

The role of instabilities in both the near-field and far-field has been considered from a variety of perspectives, both experimentally and numerically. Lignarolo *et al.*[20] conduct experiments to investigate the instabilities that lead to helical vortex breakdown in the wake of a wind turbine. The primary focus of this study is to understand how the transport and production of turbulent kinetic energy leads to the breakdown of coherent vortical structures in the wake. Wake instabilities have also considered with respect to marine propellers.[21] Large Eddy simulation (LES) is used here to investigate the development of tip vortices produced by a marine propeller with a focus on the mechanisms leading to their breakdown in the wake. More fundamental studies on vortex pair instabilities have been carried out by a number of researchers.[22–24]

Instabilities and turbulence over the tip itself have also been considered both experimentally and numerically. Using large-Eddy simulation, Jiang *et al.*[25] identify the Kelvin–Helmholtz mechanism as a primary mechanism for the generation of tip vortex instabilities. This study considers high Reynolds number flow ($Re = 4.6 \times 10^6$) and the LES is shown to capture the main physical processes when compared to experimental data.[26] Here, a primary vortex forms as a result of a shear layer roll-up on the suction side of the tip. The separated shear layer is shown to contain significant fluctuations which become entrained in the core. Crucially, it is further shown that it is the shear layers that produce the turbulence as opposed to the actual tip vortices. The experiments[26] further show that very high levels of turbulent kinetic energy are observed in the vortex core in the very near wake. This is attributed to turbulence from the boundary layer becoming entrained in the core. The two studies highlight the importance of both shear layers and boundary layers on the development and dynamics of tip vortices, particularly with regard to turbulence. The importance of shear layer instabilities is also shown experimentally by Huang and Lin.[27]

The effect of the tip flow on the lift and drag characteristics of a wing is well documented[28,29] but its influence on the dynamics of the boundary layer and hence the trailing edge flow has received less attention. Zhang *et al.*[30] use direct numerical simulations (DNSs) to investigate the tip effects on the flow over a finite-span foil and show that the dynamics of the tip flow and their interactions with the boundary layer and wake flow are strongly dependent on both aspect ratio and angle of attack. Moreau and Doolan[31] consider the role of tip flow on the overall flow field over a wing from an acoustics perspective and find that the resulting trailing edge noise is very different when comparing a finite aspect-ratio foil to one with an infinite span. Given that trailing edge noise is strongly linked to the boundary layer flow, understanding the influence of the tip flow on the boundary layer is clearly of importance. In this experimental study, the location of the boundary layer transition is shown to be strongly influenced by the aspect ratio. They also find that the tip flow influences the boundary layer and pressure distribution across the whole span, with the effective angle of attack being reduced by the tip flow. The noise produced by finite-span foil bodies has also been considered experimentally[32,33] and numerically.[34,35] However, research into the mechanisms and nature of tip vortex noise appears to be less mature than for trailing edge noise. One study[32] notes that the effect of span on noise production is minimal which contradicts the work of another,[31] where it is shown to be highly significant.

More generally, the influence of Reynolds number on the dynamics of tip-vortices and finite-span lifting surfaces is not fully understood. Most efforts to date have considered Reynolds effects in terms of the boundary layer dynamics. This has led to links being made between Reynolds number and the axial velocity in the core. Zaman *et al.*[36] compiled data from a number of sources to show that the core axial velocity generally increases with Reynolds number, with lower Reynolds number flows exhibiting wake-like cores and jet-like cores only appearing at much higher Reynolds numbers. It is suggested that wake-like cores result from thicker boundary layers becoming entrained in the vortex core, whereas jet-like cores result from higher speed flow that accelerates over the suction-side becoming entrained, leading to a higher core axial velocity than the freestream flow. A decrease in axial velocity with decreasing Reynolds number is also reported by Shekarriz *et al.*[37] Green and Acosta[38] consider Reynolds effects in their experimental study of trailing vortex dynamics and find that the influence of Reynolds number is greatest when considering the core axial velocity far downstream of the trailing edge. They find that the far-wake axial velocity increases with Reynolds number but note that the axial velocity in the near-wake is almost independent of Reynolds number. This contradicts the suggestion that this Reynolds dependence is due to the dynamics of the boundary layer.

The angle of attack also plays an important role here. In an experimental study of tip vortex dynamics over square and rounded tips,[39] it was found that jet-like cores were observed for angles of greater than 7°, with wake-like cores below this. This study further suggested that the tip geometry did not play a significant role in the determination of the core axial velocity. An increase in core axial velocity with increasing angle of attack is also reported by Green and Acosta.[38]

Numerical approaches to modeling tip vortices are diverse and some have already been discussed here. Potential flow approaches[40] or Reynolds-Averaged Navier Stokes (RANS) methods[41,42] are commonly employed to model different aspects of vortex dynamics across a range of applications. Whilst RANS methods are capable of capturing some of the large scale mean flow behavior,[43] there are significant limitations with these approaches.[44,45] Lombard *et al.*[44] highlight some of these issues and note that such approaches can lead to very large

errors in the predictions of core pressure and axial velocity. The use of more advanced turbulence models, for example, the Lag Reynolds Stress model,[46] has shown promise in the prediction of mean flow quantities but numerous deficiencies remain. Detached Eddy simulation has shown more promise in capturing vortex dynamics compared to RANS methods. Muscari *et al.*[47] investigate the vortex dynamics behind a marine propeller and show that detached Eddy simulation captures the vorticity field far better than a RANS approach with the detached Eddy simulation also capturing the onset of vortex instabilities in the wake.

The increase in computational power over the past two decades has made large Eddy simulation a more viable tool for modeling and researching complex turbulent flows. One study[48] utilizes an overset grid to investigate the tip vortex formation over a rounded tip at a high Reynolds number and good qualitative agreement with experiments is reported. LES has also been used to investigate tip vortex flows at high Reynolds numbers by Lombard *et al.*[44] who use implicit LES to investigate the flow over a wing tip at $Re = 1.2 \times 10^6$. As with Uzun *et al.*[48] and Jiang *et al.*,[25] results are compared with the experiments of Chow *et al.*[26] The results show good agreement with experiments in terms of the vortex pressure distribution and axial velocity. However, it was noted that the resolution was not adequate to fully capture the interactions of the primary and secondary vortices. In both of these studies, it is also suggested that many of the discrepancies between the experimental and numerical results are due to differences in the boundary layer. Given the very high Reynolds numbers considered here, resolving the fine turbulence scales within the boundary layer is very challenging but the lack of agreement with the experiments shows the importance of the boundary layer on the formation and dynamics of the tip vortex.

One of the main challenges with using detached-Eddy or large-Eddy simulations for tip vortex flows lies in the selection of the filter width. Because the interactions between the shear layers, vortical structures, and the boundary layer are not fully understood, it is difficult to know where a suitable cutoff point is with regard to the resolved turbulent scales. Hence, determining an appropriate filter width is difficult without performing extensive mesh sensitivity studies or detailed comparisons with first- and second-order statistical data from experiments. There are also difficulties relating to the sub-grid-scale model. This is discussed by Uzun and Hussaini[49] who compare several different models and find that the best agreement with experiments is obtained when no explicit sub-grid-scale model is used.

Far fewer studies have used DNS, primarily due to computational expense. Those that have considered relatively low Reynolds numbers, for example, Zhang *et al.*[30] who consider the flow over a finite-span wing at $Re = 400$, and Hasebe *et al.*,[50] who use DNS to assess an active control method for tip vortex suppression at $Re = 3000$. Trailing vortices have been considered in isolation or in pairs using DNS,[51,52] but it would appear that only a very small number of published studies have used DNS to fully resolve the flow over a wing-tip to date.

In this research, we perform incompressible DNSs of the flow over a flat-tipped elliptical wing at a 6 degree angle of attack. Three different Reynolds numbers (based on chord length, freestream velocity, and kinematic viscosity) are considered: $Re = 1 \times 10^4$, 4×10^4, and 1×10^5. A relatively low angle of attack is used as compared to many studies. This is chosen because many relevant geometries that produce tip-vortices operate at small angles of attack, for example, marine propellers. At higher angles of attack, increasing levels of boundary layer separation are likely and so it is of interest to understand the tip vortex dynamics for those cases where the boundary layer is likely to remain attached. The use of a flat-tipped geometry allows for the effects of tip flow separation to be investigated and to better understand how shear-layer instabilities influence both the roll-up process and the nature of the resulting trailing vortex.

DNSs have been used to provide very detailed insights into the flow physics of infinite-span wing flows,[53–56] and it is hoped that a similar level of detail and understanding can be achieved here for the flow over a finite-span wing. Due to the lack of detailed experimental data for near-field wing-tip vortex studies at low and moderate Reynolds numbers, we use three different grids for each Reynolds number in order to assess the level of grid convergence. As will be shown, the excellent level of grid independence obtained provides a high degree of confidence in the results, both for mean and time-varying quantities close to the wing and in the near-wake.

The principal aims of the study are to gain a detailed understanding of the vortex formation over a wing and to capture how this formation and the subsequent near-wake trailing vortex dynamics change with Reynolds number. The analysis considers how the tip flow develops from the leading edge over the length of the tip. The range of Reynolds numbers covered enables the role of instabilities and transition to be investigated in detail, with the origin of turbulent instabilities being discussed as well as their influence on the tip flow.

The changes in properties such as core pressure and turbulence intensity as the Reynolds number increases are of particular interest to those developing scaling laws for important phenomena such as cavitation inception and tip vortex noise.

Simulations are also conducted for an infinite aspect-ratio wing which allows for the influence of the tip flow on the surface pressure and boundary layer to be investigated.

II. METHODS

A. Governing equations and numerical methods

The governing equations for an incompressible Newtonian fluid are given in Eqs. (1) and (2),

$$\frac{\partial U_i}{\partial x_i} = 0, \tag{1}$$

$$\frac{\partial U_j}{\partial t} + U_i \frac{\partial U_j}{\partial x_i} = -\frac{1}{\rho}\frac{\partial p}{\partial x_j} + \nu \frac{\partial^2 U_j}{\partial x_i^2}. \tag{2}$$

A second-order, three-point backward scheme is used for the discretization of the time derivative. Second-order central schemes are used for the spatial derivatives. The coupled pressure/velocity fields are solved at each time step using the PISO algorithm[57] with an algebraic multi-grid solver for the pressure correction equation.[58] Fully implicit convergence is achieved at each time step to a level of 1×10^{-6} for the normalized residuals for both the pressure and velocity fields. The time steps for each simulation are chosen to ensure that the Courant number is less than 1. The finite volume platform OpenFOAM is used for the implementation of these algorithms.

B. Geometry and meshing

The geometry used for this study is an elliptical wing with a chord of 0.3 m. The maximum thickness is 10% of the chord length

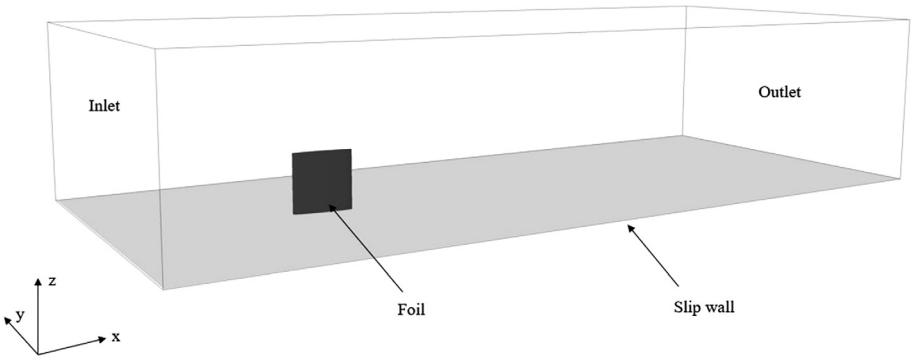

FIG. 1. Fluid domain for the finite aspect-ratio cases.

and the span is equal to the chord length. The geometry has a flat tip and constant thickness profile along the span.

The domain extends 3 chord-lengths upstream of the leading edge and 12 chord-lengths downstream. The side walls are placed at 3 chord-lengths away from the wing and the top is 2 chord lengths above the wing tip in the case of the finite-aspect ratio wing simulations. The fluid domain and co-ordinate system are shown in Fig. 1. Block-structured meshes consisting of hexahedral cells are used throughout. The meshes are designed around x_i^+ values, estimated using a Blasius boundary layer formula, and a downstream refinement. The downstream refinement extends to 3 chord-lengths downstream of the trailing edge, beyond which the mesh is coarsened. The wake refinement is based on a target cell size in the axial direction and is given as a percentage of the chord length (see Table I). The mesh is coarsened significantly toward the far-field boundaries to increase dissipation in these regions.

For the lowest Reynolds number, the mesh resolution is driven by the need to capture pressure and velocity gradients as opposed to turbulent structures. For the finite-span simulations, the span-wise resolution is graded such that the resolution at the tip is finer than at the symmetry plane, resulting in a wall normal resolution at the tip of $x_n^+ \leq 1$.

TABLE I. Mesh parameters. The non-dimensional cell sizes in the chord-wise, wall-normal and span-wise directions are denoted by x^+, y^+, and z^+, respectively. AR denotes the geometric aspect ratio.

$Re(-)$	AR	Mesh	N cells ($\times 10^6$)	x^+	y^+	z^+	Wake (%chord)
1×10^4	1	Coarse	12.4	6.4	0.9	10	2.0
1×10^4	1	Medium	20.7	4.8	0.9	6	1.0
1×10^4	1	Fine	39.9	3.2	0.9	5	0.5
4×10^4	1	Coarse	22.9	18	0.8	18	2.0
4×10^4	1	Medium	45.8	14	0.8	14	1.0
4×10^4	1	Fine	93.5	9	0.8	9	0.5
1×10^5	1	Coarse	23.3	26	1.2	36	2.0
1×10^5	1	Medium	71.2	16	0.9	18	1.0
1×10^5	1	Fine	126.2	12	0.9	12	0.5
1×10^5	∞	Coarse	11.3	26	1.2	36	2.0
1×10^5	∞	Medium	31.7	16	0.9	18	1.0
1×10^5	∞	Fine	69.5	12	0.9	12	0.5

C. Boundary and initial conditions

A fixed value boundary condition is applied to the velocity field at the inlet and a Neumann condition is applied at the outlet. A Neumann boundary condition is applied to the pressure field at the inlet with a Dirichlet condition at the outlet. The top, bottom, and sides of the domain are defined as slip walls, with no-slip condition being applied to the wing. The boundary condition applied at the bottom results in an effective aspect ratio of 2 for the wing.

Simulations using the coarsest mesh for each Reynolds number have been run for 20 chord-flow times to allow for the flow-field to develop to a statistically stationary state. In order to reduce the computation times required for medium and fine meshes, the results from the coarse meshes are mapped onto these meshes to provide the initial conditions. The medium and fine meshes are then run for a further 20 chord-flow times.

III. RESULTS

A. Presentation of results

In order to analyze both the mean and unsteady flows over the tip and in the near wake, the pressure and velocity fields have been saved at a number of chordwise locations over the wing and up to three chord-lengths downstream of the trailing edge. Over the tip and the very near wake (up to 0.1c downstream of the trailing edge), a spatial resolution of 2×10^{-4} m is used and a resolution of 2.5×10^{-3} m is used in the wake. Velocity data are normalized by the freestream velocity and pressure data are presented in the form of a pressure coefficient: $C_p = p/(0.5\rho\bar{U}^2)$. A number of contour plots are presented in the following sections and an example of how these should be interpreted is given in Fig. 2. Unless otherwise stated, the results presented are for the most resolved meshes for each Reynolds number.

Coherent vortical structures are identified using the Q-criterion[59] and also the $\hat{Q}$-criterion.[60] By decomposing the velocity gradient tensor into symmetric and non-symmetric parts, we can identify regions of flow dominated by either straining or vorticity. We define the rate-of-strain tensor as

$$\mathbf{S} = \frac{1}{2}(\nabla \mathbf{U} + (\nabla \mathbf{U})^T). \tag{3}$$

The vorticity tensor is defined by

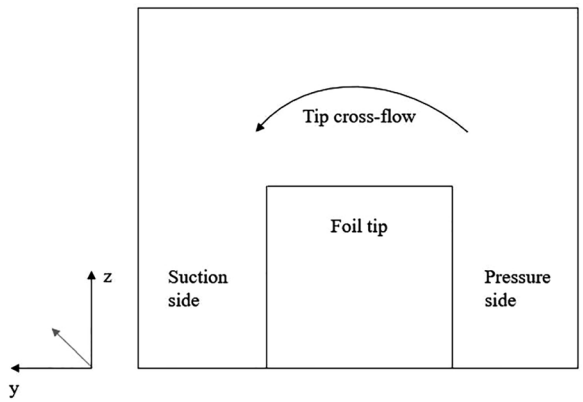

FIG. 2. Sample contour plot.

$$\Omega = \frac{1}{2}(\nabla \mathbf{U} - (\nabla \mathbf{U})^T). \tag{4}$$

From these, we can define the Q-criterion as

$$Q = \frac{1}{2}(||\Omega||^2 - ||\mathbf{S}||^2), \tag{5}$$

where $||\mathbf{S}|| = S_{ij}S_{ij}$ and $||\Omega|| = \Omega_{ij}\Omega_{ij}$. To allow for comparisons to be more easily made between the different cases, the normalized Q-criterion is also used, as defined in equation 6. This varies between -1 and 1, with -1, 0, and 1 denoting vortical, straining, and irrotational regions, respectively,

$$\hat{Q} = \frac{||\mathbf{S}||^2 - ||\Omega||^2}{||\mathbf{S}||^2 + ||\Omega||^2}. \tag{6}$$

Throughout this study, a vortex core is defined as the location of minimum pressure for which $\hat{Q} < -0.5$. Due to oscillations in the lateral and vertical position of the vortex core, the pressure and velocity data in the core are obtained by locating the minimum pressure at each time step.

Fluctuating or turbulent flow is largely presented using the turbulence intensity which, being a percentage of the mean flow, allows for easier comparisons to be made between the different cases,

$$I = \frac{\sqrt{2k/3}}{U_\infty}, \tag{7}$$

where k denotes the turbulent kinetic energy, defined by

$$k = \frac{1}{2}u'_{ii}. \tag{8}$$

Fluctuations that are indicative of unsteady or transitional flow are also presented in this manner. In general, the term *fluctuation intensity* will be used in relation to fluctuating flow that is broadly coherent, whereas *turbulence intensity* will be used for regions of flow where the fluctuations are more broadband and stochastic. It should be noted, however, that the calculation is the same for both. This is done to allow for a more direct comparison of the energy levels within the flow during and after the transition to turbulence.

B. Overview of results

Before undertaking a more detailed analysis of the results, an overview is presented here outlining the general flow features of each case.

The vortex development over the tip of the wing varies considerably as the Reynolds number increases. These differences can clearly be seen in Fig. 3, which shows contour plots of $iso - \hat{Q}$ for each of the three Reynolds numbers. At the lowest Reynolds number, it can be seen that the vortex roll-up takes place just downstream of the trailing edge and no vortical structures are identified over the tip of the wing. Laminar vortices are shed from the trailing edge, which are strongly influenced by the presence of the tip flow. For the two higher Reynolds numbers, multiple vortical structures are identified over the wing, and the flow in the wake appears turbulent. The influence of the tip flow on the trailing edge flow appears to diminish with increasing Reynolds number. There are clear similarities between the flow at $Re = 4 \times 10^4$ and $Re = 1 \times 10^5$ but there are also important differences, which are explored further throughout the results.

The development of the multiple vortices over the tip can be seen clearly in Fig. 4, which shows contour plots of the axial velocity and $\hat{Q}$ over the tip at $Re = 4 \times 10^4$. Multiple vortices with wake-like cores can be identified, with the axial velocity contours suggesting that flow separation over both the pressure and suction sides of the tip is playing an important role in the development of these wake-like vortical structures. This is discussed in greater detail in Sec. IV.

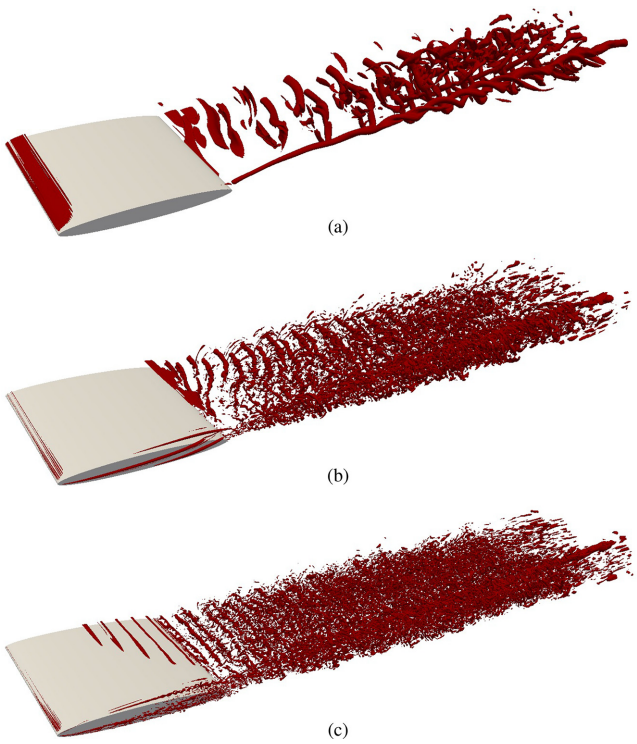

FIG. 3. Instantaneous $iso - \hat{Q}$ contours for $\hat{Q} = -0.5$ at each of the three Reynolds numbers. (a) $Re = 1\times 10^4$, (b) $Re = 4\times 10^4$, and (c) $Re = 1\times 10^5$.

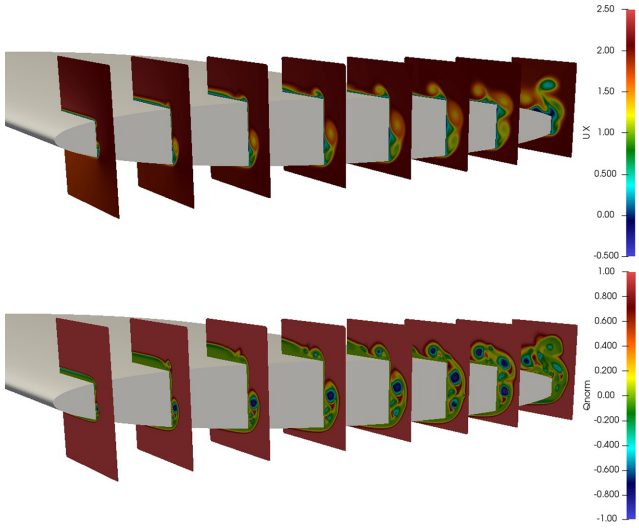

FIG. 4. Contour plots of instantaneous axial velocity ($m\,s^{-1}$) (top) and $\hat{Q}(-)$ (bottom) over the wingtip at $Re = 4 \times 10^4$.

An initial assessment of the level of mesh independence of the results at the three Reynolds numbers can be obtained by comparing the mean and root mean square (RMS) values for the lift and drag. These are shown in Figs. 5 and 6 which show excellent agreement, particularly when considering the medium and fine meshes. As expected, an increase in Reynolds number leads to a decrease in the drag coefficient, with the RMS values increasing with Reynolds number, implying greater levels of unsteadiness in the flow.

The boundary layers for the two lowest Reynolds numbers are fully laminar, whereas the suction-side boundary layer is transitional at the highest Reynolds number. It can be seen in Fig. 3 that transition begins earlier further away from the tip, implying that the tip flow is influencing the boundary layer dynamics. Figure 7 shows the power spectral densities of the chord-wise velocity fluctuations in the boundary layer, highlighting growing fluctuations centered around a 65 Hz component. This behavior indicates the presence of Tollmien-Schlichting waves and is considered in more detail in Sec. III E. The results shown here further demonstrate excellent levels of agreement between the different grids, with all three capturing the same amplitude and frequency of the instability wave.

Further comparisons between the different grid resolutions are presented in subsequent sections including for the wake flow in Sec. III D and the boundary layer in Sec. III E.

C. Vortex development over the tip

In this section, the vortex development and dynamics over the tip are described in more detail, focusing initially on the two higher Reynolds numbers.

Close to the tip leading edge, a vortex forms rapidly with a single coherent structure being identified at around $0.02c$ downstream of the leading edge. The mean behavior of the flow is similar at both Reynolds numbers. A large deficit in axial velocity is observed, which is due to flow separation at the tip leading edge. A recovery in both pressure and axial velocity is then observed over the first part of the wing. Figure 8 shows the normalized axial velocity and pressure coefficient of the vortex core over the first half of the wing. The velocity deficit close to the leading edge is similar at both Reynolds numbers but recovers more quickly at the $Re = 1 \times 10^5$.

Figures 9 and 10 show how the primary vortex forms close to the leading edge by considering how the pressure changes over the first part of the wing. The same features can be identified for both Reynolds numbers, but the core pressure is significantly lower at the higher Reynolds number. The pressure is at a minimum very close to the leading edge for $Re = 1 \times 10^4$, whereas at the higher Reynolds number this is reached at around 0.1c downstream of the leading edge. The rapid formation of the vortex is the result of flow separation due to the geometry of the tip. The flow separates at the tip leading edge on the pressure side leading to a shear layer that rolls up to form the vortex.

The way in which this first vortex forms suggests a strong dependence on the tip geometry. The vortex forms because of the separation induced by the flat tip, which agrees qualitatively with the experimental results presented by Ref. 3. In their study, smoke visualization of the flow over a flat-tipped wing reveals similar flow patterns, with separation over the pressure-side of the tip leading to the formation of vortices on the tip. This contrasts with the results from experiments using a rounded tip, where vortices form only on the suction side of the wing.

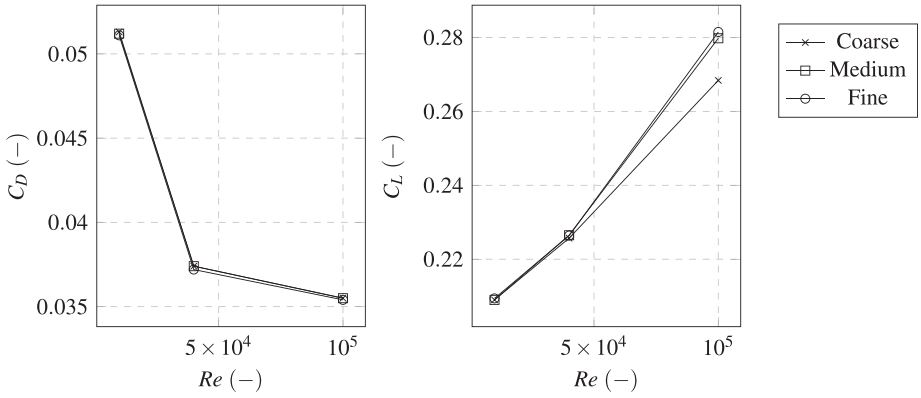

FIG. 5. Mean drag and lift coefficients as a function of mesh resolution and Reynolds number.

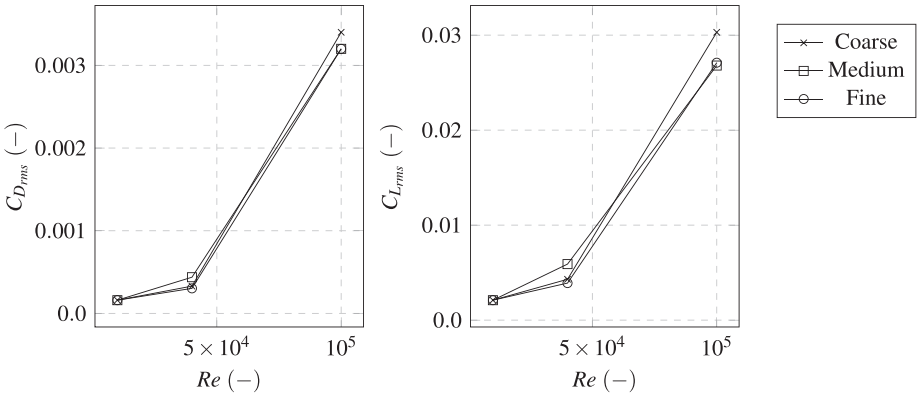

FIG. 6. Root-mean square drag and lift coefficients as a function of mesh resolution and Reynolds number.

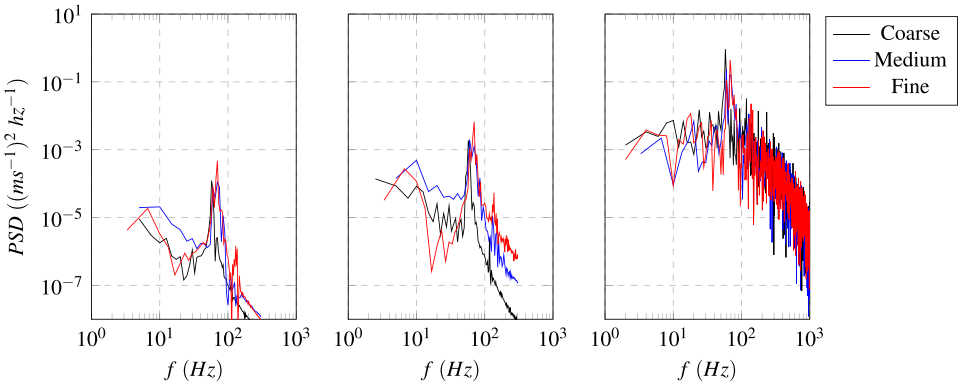

FIG. 7. Power spectral densities of chordwise velocity fluctuations in the boundary layer for $s = 0.2c$ at $x/c = 0.6$ (left), $x/c = 0.8$ (center), and $x/c = 1.0$ (right) for the finite-span case at $Re = 1 \times 10^5$.

Whilst the mean flow exhibits similar behavior at the two higher Reynolds numbers, there are substantial differences in the nature of the unsteady flow. At $Re = 4 \times 10^4$, the vortex that forms at the leading edge is laminar but at $Re = 1 \times 10^5$ a transition takes place. The shear layer is unstable here, leading to the flow becoming turbulent. Rapidly growing fluctuations are observed with a dominant frequency of 956 Hz. The vortex roll-up happens more rapidly than the transition but the flow in the vortex core does eventually become fully turbulent, as shown in Figs. 11 and 12.

The relationship between the transitional flow over the tip and the vortex can be seen by looking at the intensity of the velocity fluctuations just downstream of the leading edge. Figure 11 shows the fluctuation intensities at $0.03c - 0.05c$ downstream of the leading edge. The fluctuations originating in the shear layer [see Fig. 11(a)] grow in amplitude and become wrapped around the vortex [Fig. 11(b)], before becoming entrained in its core. The intensity of the fluctuations is very high in this region, with the RMS in excess of 16% of the freestream velocity.

These dynamics result in the vortex core becoming fully turbulent slightly further downstream than the flow surrounding it. Spectral analysis of the velocity fluctuations in the core show that they retain a more coherent structure for longer than in the surrounding fluid.

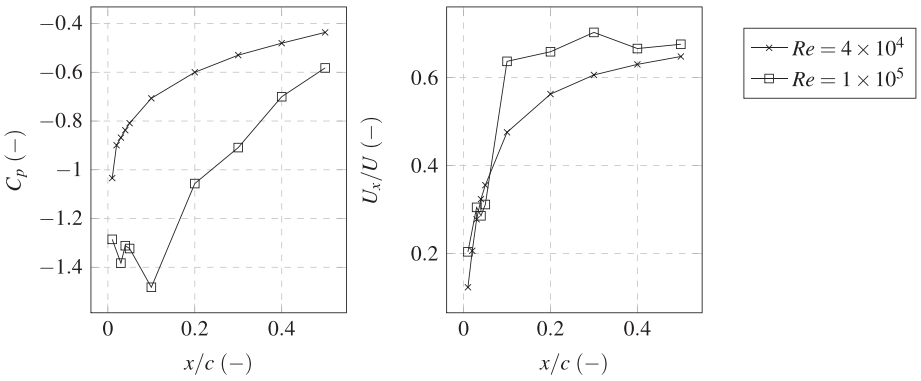

FIG. 8. Pressure coefficient and axial velocity in the vortex core for $Re = 4 \times 10^4$ and $Re = 1 \times 10^5$.

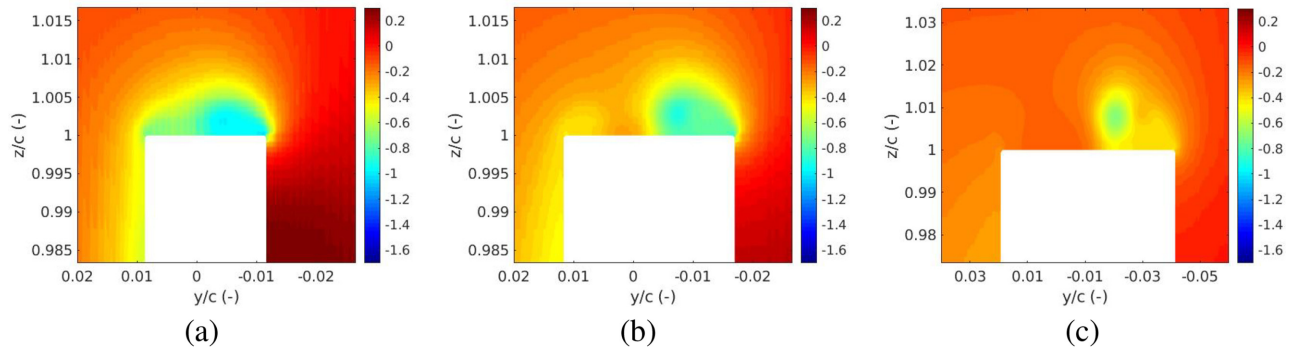

FIG. 9. Mean pressure coefficient contours at $x/c = 0.01,\ 0.02,\ 0.1$ for $Re = 4 \times 10^4$. (a) $x/c = 0.01$, (b) $x/c = 0.02$, and (c) $x/c = 0.1$.

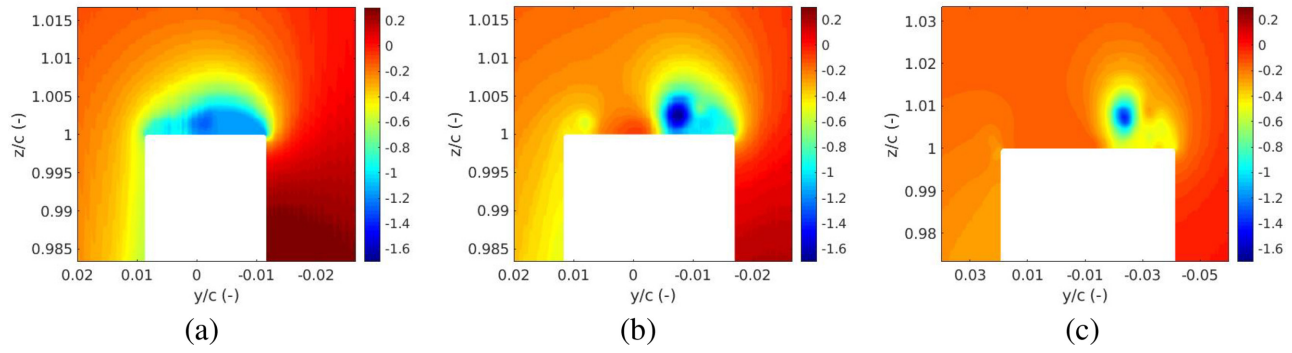

FIG. 10. Mean pressure coefficient contours at $x/c = 0.01,\ 0.02,\ 0.1$ for $Re = 1 \times 10^5$. (a) $x/c = 0.01$, (b) $x/c = 0.02$, and (c) $x/c = 0.1$.

However, by $x/c = 0.3$, the fluctuations both in the core and in the surrounding fluid have lost their initial structure, dominated by the 956 Hz component, and the flow can be considered fully turbulent. This can be seen in Fig. 12 which shows the power spectral densities of the axial velocity fluctuations both in the vortex core and in the shear layer. At $x/c = 0.2$, the core fluctuations are still dominated by the narrowband component that exists in the transitional shear layer further upstream, whereas the shear layer no longer contains any narrowband component. The Reynolds stresses in the vortex core peak before this, coinciding with the location of minimum pressure, at $x/c = 0.1$.

At around 30% chord length downstream of the leading edge, additional structures start to form. At both $Re = 4 \times 10^4$ and $Re = 1 \times 10^5$, a vortex forms due to flow separating as it passes over

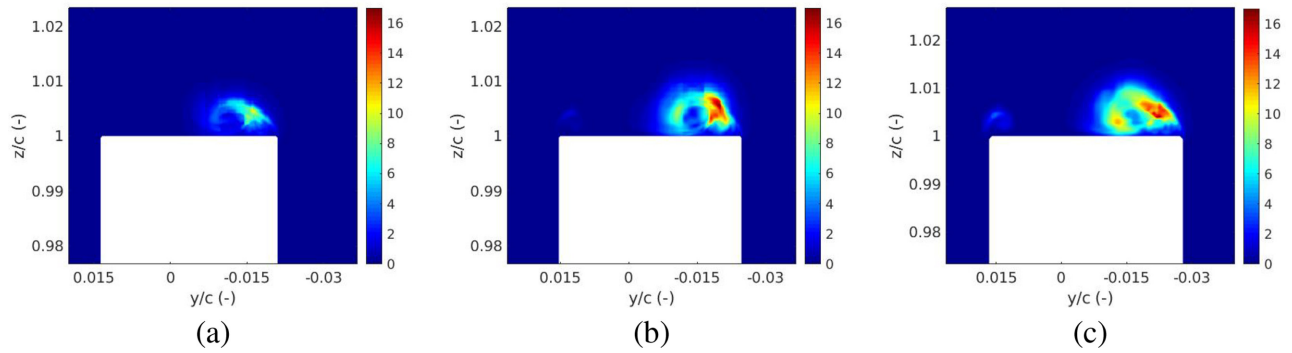

FIG. 11. Fluctuation intensities of the tip flow at $x/c = 0.03,\ 0.04,\ 0.05$ for $Re = 1 \times 10^5$. (a) $x/c = 0.03$, (b) $x/c = 0.04$, and (c) $x/c = 0.05$.

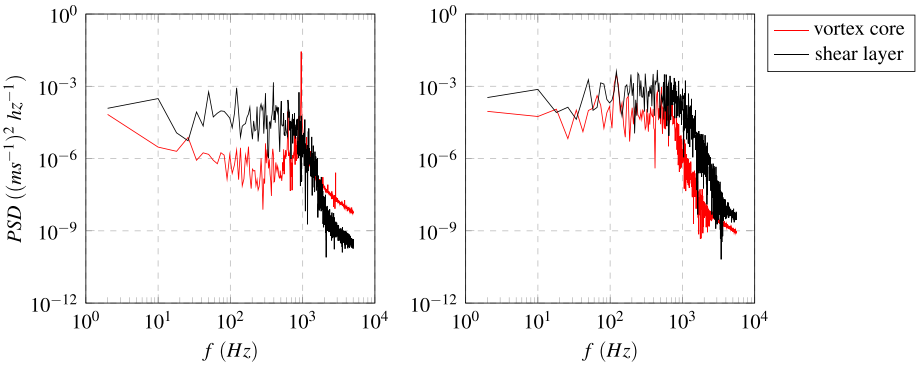

FIG. 12. Power spectral density of chordwise velocity fluctuations in the vortex core and shear layer at $x/c = 0.2$ (left) and $x/c = 0.3$ (right) for $Re = 1 \times 10^5$.

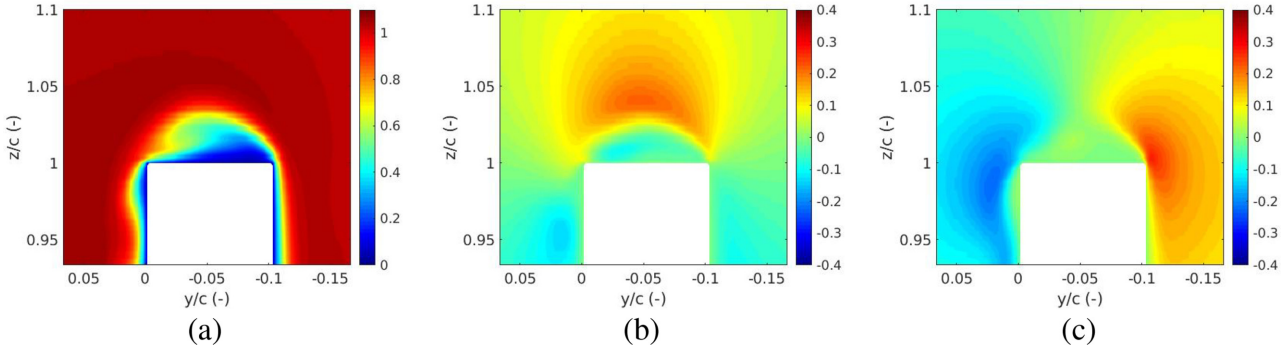

FIG. 13. Mean velocity $(U_x, U_y, U_z)/U_\infty$ contours at $x/c = 0.5$ for $Re = 1 \times 10^4$ normalized by freestream velocity. (a) U_x/U_∞, (b) U_y/U_∞, and (c) U_z/U_∞.

the tip to the suction side. In addition to this, another vortex starts to form over the tip on the pressure side of the primary vortex. This vortex is more coherent at $Re = 4 \times 10^4$, which may be due to the laminar nature of the flow here. The turbulence intensity at the highest Reynolds number in this region is over 10%, which may be preventing the formation of a distinct vortical structure.

Figures 13–15 show the mean velocity contours at mid-chord for each of the three Reynolds numbers. The contour plots for the lowest Reynolds number show the flow separating at the pressure side of the tip and reattaching on the suction side below the tip. As with the flow at the leading edge, the two higher Reynolds numbers exhibit similar mean behavior, with a complex structure over the tip and a secondary vortex clearly visible on the suction side of the wing.

The relationship between the boundary layer and the vortex should also be noted here, particularly when considering the core axial velocity. At the lower Reynolds numbers, the boundary layer is thicker and it has been suggested that this results in a positive correlation between Reynolds number and axial velocity. In these results, it has been shown that the wake-like vortex core over the tip is actually due to flow separation at the tip-leading edge, which is a combination of both the geometry and Reynolds number. These findings agree with Zaman *et al.*,[36] who note that both geometry and operating conditions

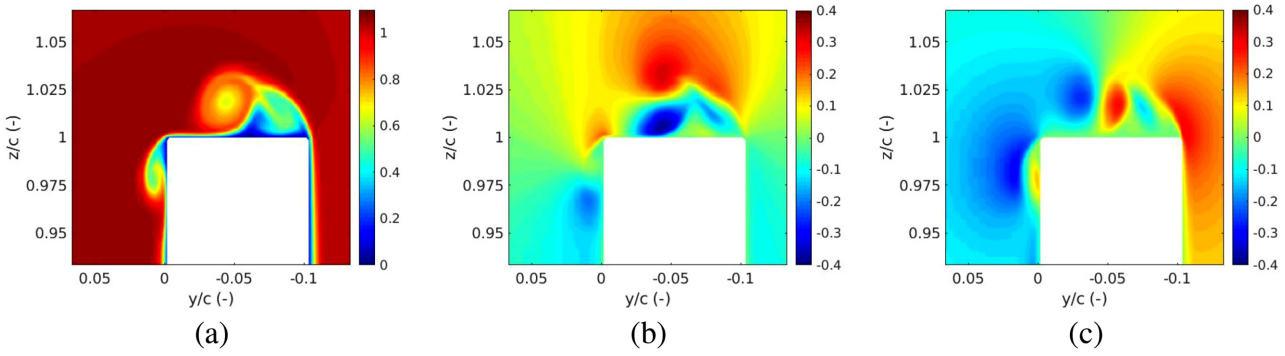

FIG. 14. Mean velocity $(U_x, U_y, U_z)/U_\infty$ contours at $x/c = 0.5$ for $Re = 4 \times 10^4$ normalized by freestream velocity. (a) U_x/U_∞, (b) U_y/U_∞, and (c) U_z/U_∞.

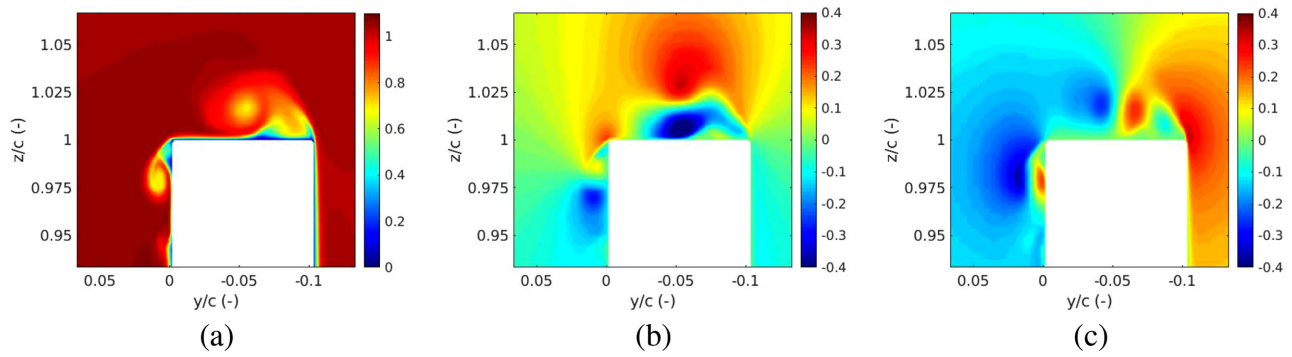

FIG. 15. Mean velocity $(U_x, U_y, U_z)/U_\infty$ contours at $x/c = 0.5$ for $Re = 1 \times 10^5$ normalized by freestream velocity. (a) U_x/U_∞, (b) U_y/U_∞, and (c) U_z/U_∞.

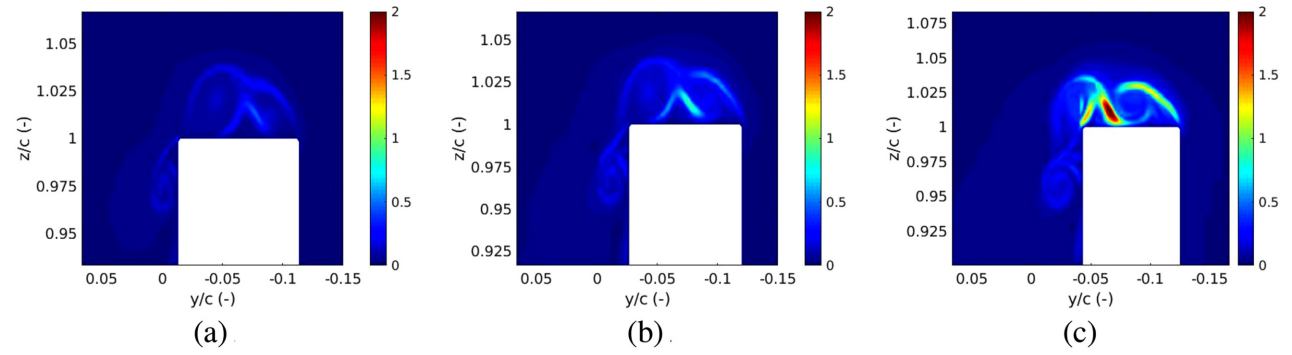

FIG. 16. Fluctuation intensities at $x/c = 0.6, 0.7, 0.8$ for $Re = 4 \times 10^4$. (a) $x/c = 0.6$, (b) $x/c = 0.7$, (c) $x/c = 0.8$.

play a role here. However, the results contrast with those of Lee and Pereira,[39] who suggested that geometry did not play a significant role in the determination of core axial velocity in their experimental study of tip vortex flows at different angles of attack at $Re = 3.07 \times 10^5$.

Moving further downstream, growing fluctuations are observed in the different shear layers for $Re = 4 \times 10^4$. The first is the layer that forms due to the separation of flow as it passes over the tip from the pressure side. Small fluctuations are present in the shear layer on the suction side of the tip but these do not grow over the chord length. The most interesting are the fluctuations that exist around the two co-rotating vortices on the tip. In Fig. 16, growing fluctuations can be seen around the vortices, with the largest growth occurring in the shear layer that exists between them. As with the primary vortex, the shear layer that forms when fluid separates as it passes over to the suction side is unstable at $Re = 1 \times 10^5$. This leads to the secondary vortex becoming turbulent in the same manner as the primary vortex at this Reynolds number. This can clearly be seen in Fig. 17, which also shows the strongly turbulent flow on the tip.

As the vortices move closer to the trailing edge, they begin to merge on the suction side of the wing, as shown in Figs. 18 and 19.

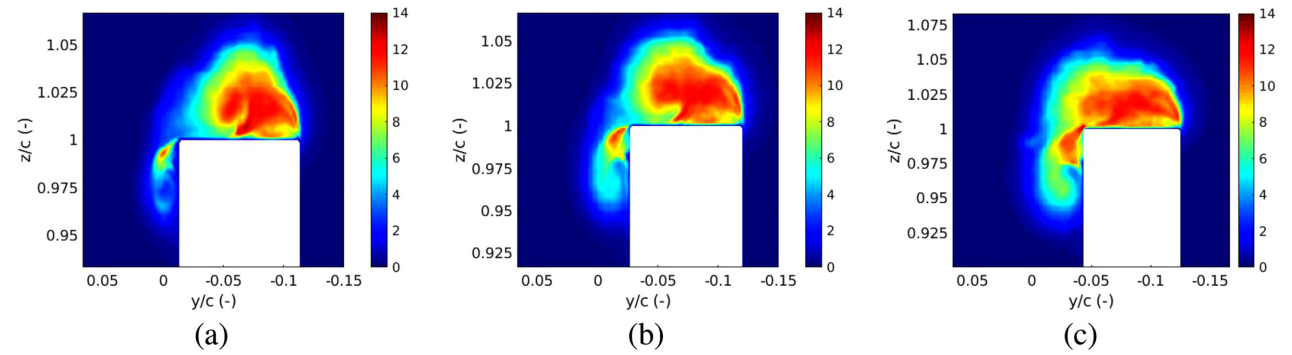

FIG. 17. Turbulence intensities at $x/c = 0.6, 0.7, 0.8$ for $Re = 1 \times 10^5$. (a) $x/c = 0.6$, (b) $x/c = 0.7$, and (c) $x/c = 0.8$.

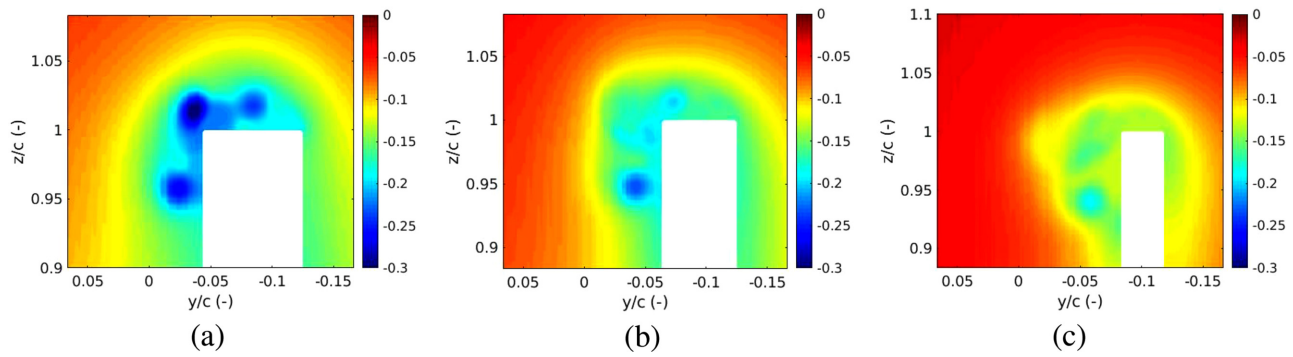

FIG. 18. Mean pressure coefficient at $x/c = 0.8, 0.9, 0.97$ for $Re = 4 \times 10^4$. (a) $x/c = 0.8$, (b) $x/c = 0.9$, (c) $x/c = 0.97$.

The pressure recovery in the primary vortex over the tip is greater than that of the secondary vortex such that the lowest pressure is now seen in the secondary vortex immediately prior to merging. The primary vortex then moves over to the suction side and merges with the secondary vortex. The pressure in the vortical structures continues to increase throughout this process. The vortex merging happens more rapidly at the higher Reynolds number, with a single vortical structure emerging upstream of the trailing edge.

For $Re = 4 \times 10^4$, as the two co-rotating structures move over to the suction side, the fluctuating flow between them separates off and becomes entrained in the center of the merging structures. The flow becomes increasingly turbulent during this process, with the pressure-side shear layer becoming a significant source of turbulent kinetic energy.

At the lowest Reynolds number, the roll-up process starts to take place at the trailing edge. The boundary layer over the chord thickens considerably here and a recirculation bubble forms on the suction side. As the geometry narrows toward the trailing edge, the flow over the tip starts to wraparound this recirculating flow with the roll-up process completing downstream of the trailing edge. This leads to the axial velocity in the core being *negative* in the near wake, as shown in Fig. 20.

At $x/c = 0.1$ downstream of the trailing edge, a single trailing vortex is present at all Reynolds numbers (see Fig. 21). The vortex at $Re = 1 \times 10^4$ has a much larger diameter than is seen at higher Reynolds numbers and this reflects the different nature of its formation. The vortex cores for the two higher Reynolds numbers are turbulent. At $Re = 4 \times 10^4$, the process of vortex merging is still happening at the trailing edge and this results in boundary layer flow at the trailing edge becoming entrained in the resultant vortex. This increases the turbulence intensity in the vortex core. Despite the different nature of the vortex formation across the range of Reynolds numbers, the axial velocity and the pressure in the vortex cores follow a clear trend, with lower Reynolds numbers resulting in a large velocity deficit and higher Reynolds numbers leading to lower core pressures.

D. Near-wake dynamics

In the near-wake, the tip vortex formed at $Re = 1 \times 10^4$ shrinks in diameter and the pressure in the core drops to a minimum at around 1 chord length downstream. By this point, the axial velocity has recovered to around 50% of the freestream velocity, as shown in Fig. 22. At higher Reynolds numbers, the initial recovery in axial velocity is sharp but then tapers off over the next few chord lengths downstream, as shown in Figs. 23 and 24. These figures also compare these values for the different mesh resolutions and generally show excellent agreement, particularly between the medium and fine meshes. The coarse meshes generally show a faster recovery in the core pressure, which may be due to the increased dissipation present in the coarser simulations, which causes the vortex to decay prematurely.

The decay in turbulence intensity in the core for the two higher Reynolds numbers is shown in Fig. 25. A similar trend is observed

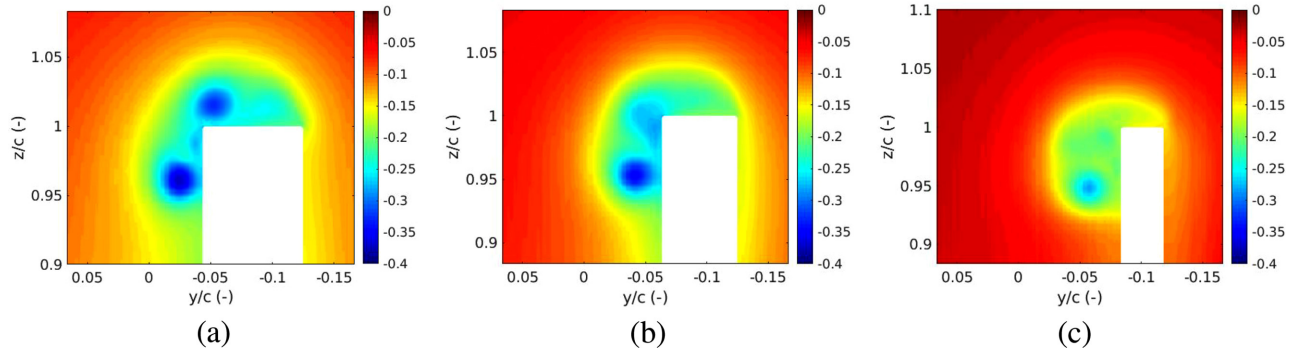

FIG. 19. Mean pressure coefficient at $x/c = 0.8, 0.9, 0.97$ for $Re = 1 \times 10^5$. (a) $x/c = 0.8$, (b) $x/c = 0.9$, and (c) $x/c = 0.97$.

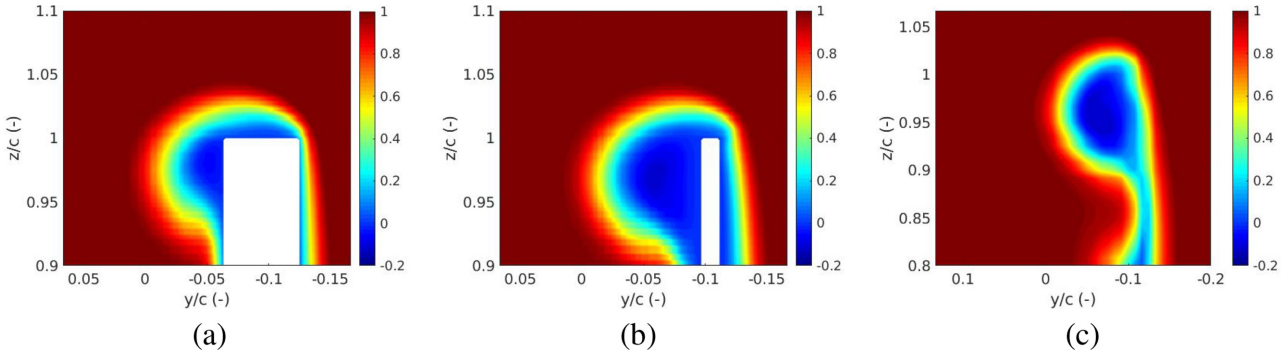

FIG. 20. Mean axial velocity (U_x) contours at $x/c = 0.9,\ 0.99,\ 1.1$ for $Re = 1 \times 10^4$. (a) $x/c = 0.9$, (b) $x/c = 0.99$, and (c) $x/c = 1.1$.

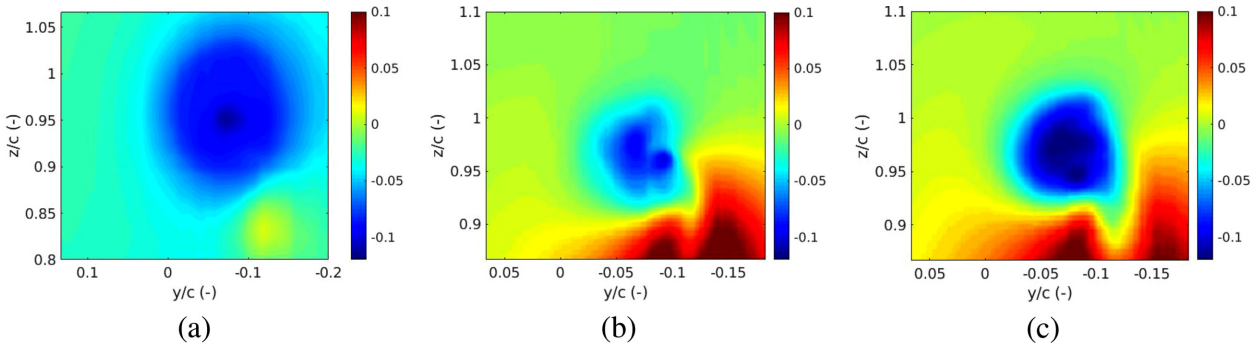

FIG. 21. Mean pressure contours at $x/c = 1.1$ for $Re = 1 \times 10^4$, $Re = 4 \times 10^4$, and $Re = 1 \times 10^5$.

here, with a sharp initial fall in intensity followed by a more gradual decay. Results are again shown for all meshes, with the coarsest mesh showing an under-prediction in the turbulence intensity compared to the medium and fine meshes, which show good agreement at both Reynolds numbers.

At first glance, turbulence intensities in Fig. 25 appear to contradict the results presented in the previous section. Despite a largely laminar flow at $Re = 4 \times 10^4$ over the wing, the turbulence intensity in the trailing vortex is just as high as for $Re = 1 \times 10^5$ which had significant levels of turbulence over the tip. This can be explained by the fact that the roll-up of the vortex at the lower Reynolds number takes place slightly later. As a result, the roll-up process is still taking place at the trailing edge allowing for turbulent boundary layer material to be entrained within the core. This results in a different pattern being observed in the Reynolds stresses. At the higher Reynolds number, the Reynolds stresses peak immediately before the trailing edge and then decay sharply. At $Re = 4 \times 10^4$, the stresses peak downstream of the trailing edge and decay more slowly.

At the lowest Reynolds number, $Re = 1 \times 10^4$, a very different behavior is observed in the trailing vortex. As the vortex propagates downstream, growing fluctuations are observed in the core. These fluctuations grows to a maximum at around $x/c = 2.6$ at which point the

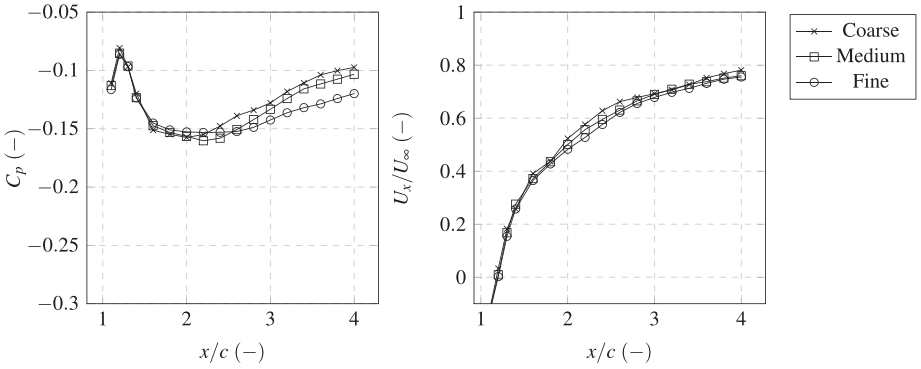

FIG. 22. Mean pressure coefficient and axial velocity in the trailing vortex at $Re = 1 \times 10^4$.

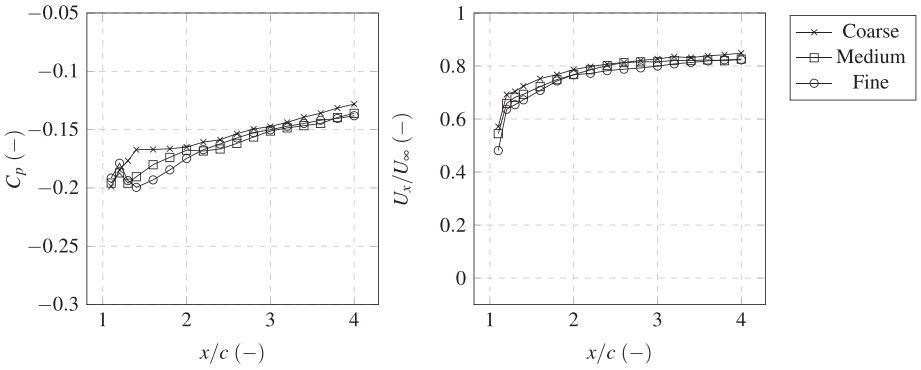

FIG. 23. Mean pressure coefficient and axial velocity in the trailing vortex at $Re = 4 \times 10^4$.

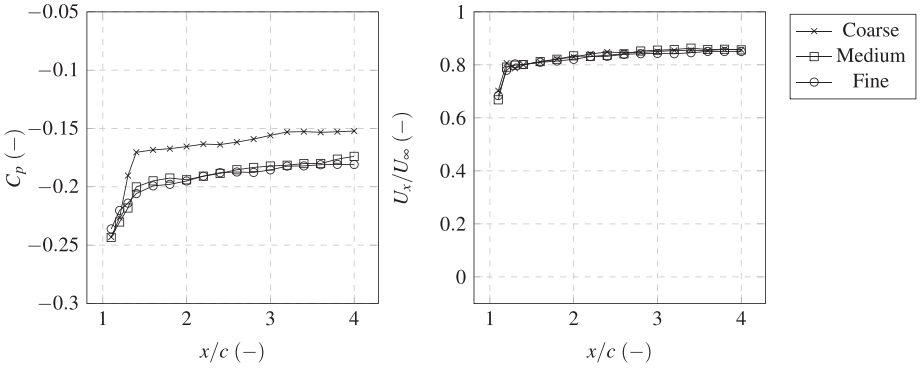

FIG. 24. Mean pressure coefficient and axial velocity in the trailing vortex at $Re = 1 \times 10^5$.

vortex splits into two structures that wind around each other, as shown in Fig. 26. The power spectral densities of the axial velocity fluctuations in the core show growing fluctuations dominated by a narrowband component with a frequency of 3.8 Hz, which is the same as the trailing edge vortex shedding frequency. This can be explained by noting that the trailing vortex formed from tip flow wrapping around the region of separated flow close to the trailing edge. This bubble contained a small fluctuating component associated with the periodic laminar shedding at the trailing edge and it is this fluctuation that grows as the trailing vortex propagates downstream. This behavior contrasts sharply with the two higher Reynolds numbers, which show decaying levels of turbulence in the vortex. The differences reflect the different ways in which the vortices form upstream, which highlights the importance of accurately resolving the vortex formation over the tip in order to understand the dynamics in the wake.

E. Influence of the tip vortex on surface pressure and boundary layer dynamics

It is well known that a finite-span wing will have a lower lift to drag ratio than its infinite-span equivalent. The tip flow reduces the effective angle of attack of the wing, thus reducing the pressure differential between the pressure and suctions sides. In order to better understand the influence of the tip flow on both the surface pressure and boundary layer dynamics, three additional simulations have been run at $Re = 1 \times 10^5$ with an infinite aspect ratio wing using symmetry

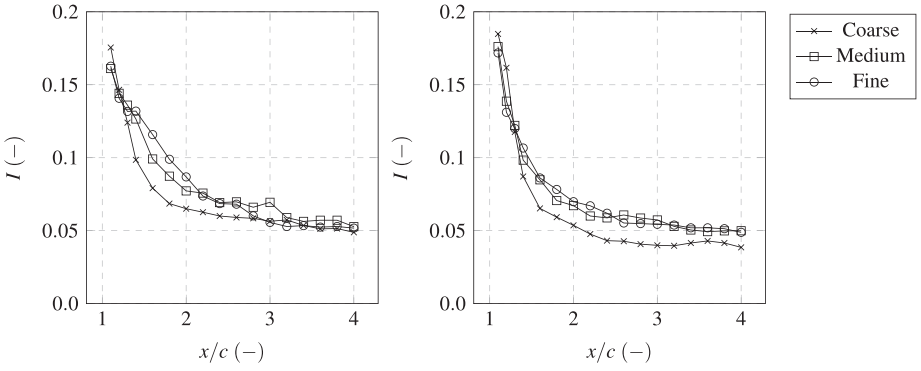

FIG. 25. Turbulence intensity in the vortex core in the wake for $Re = 4 \times 10^4$ (left) and $Re = 1 \times 10^5$ (right).

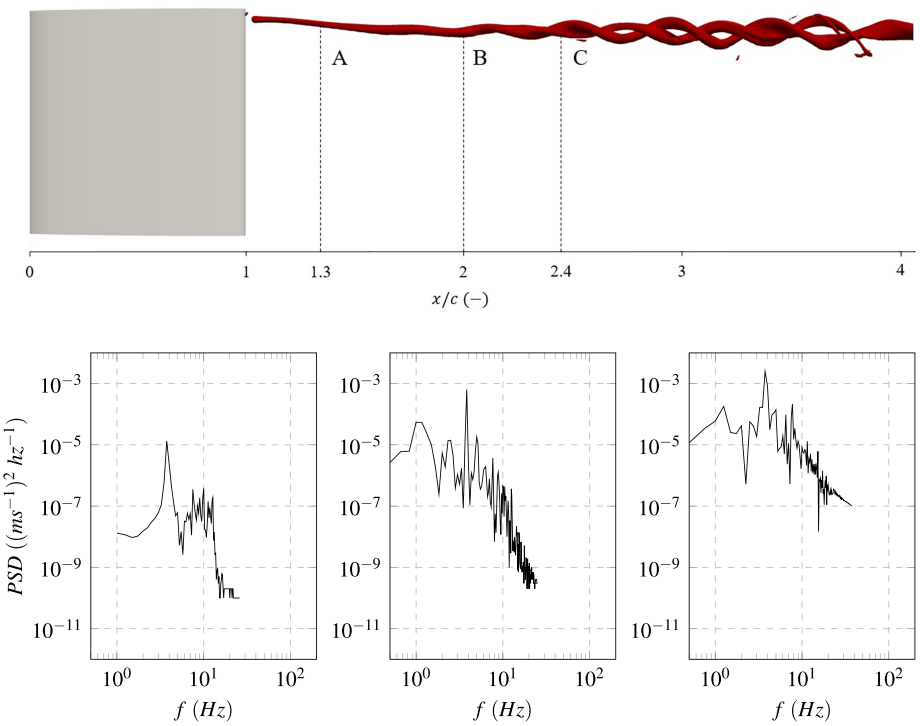

FIG. 26. Visualization of the tip vortex at $Re = 1 \times 10^4$ using iso contours of $\hat{Q} = -0.5$ together with the power spectral densities of the axial velocity at locations A (left), B (center) and C (right).

boundary conditions at either end. The geometric aspect ratio remains the same as for the finite-span simulations to allow for a more direct comparison. The simulations have been run using the same mesh resolutions as their finite-span counterparts, again to allow for a more direct comparison and to provide greater confidence in the results. In the following analysis, a span-wise location of $s = 0.0c$ denotes the symmetry plane and $s = 1.0c$ denotes the tip.

A comparison of the surface pressure distributions between the finite and infinite-span cases is shown in Fig. 27. This shows a large difference in both the magnitude and also the shape of the pressure distribution. The initial pressure drop at the leading edge for the infinite-span is larger in magnitude and is sustained over a greater length, indicating flow separation at the leading edge. For the finite-span case, the pressure drop is lower at all span-wise locations, with the pressure drop reducing toward the tip. The pressure distribution does not indicate flow separation at any span-wise location. There is a modest change in the pressure distribution at the two span-wise locations, but both are significantly different from the infinite-span case. The changes in the pressure have considerable impact on the lift, with the infinite-span wing having a lift coefficient 2.3 times larger than the finite-span wing. The results compare qualitatively well to those presented by Ref. 31. In their experimental study of flow over a wall-mounted wing, it is shown that the effective angle of attack is reduced across the entire span. It is also shown in this study that the aspect ratio plays an important role here, with smaller aspect ratios experiencing a large reduction in effective angle of attack due to the larger relative size of the tip flow scales.

The change in effective angle of attack also has an important effect on the boundary layer. It was shown in the results overview that the boundary layers at the two lowest Reynolds numbers remain laminar, whereas the suction-side boundary layer at the highest Reynolds number is transitional. Based on existing studies of infinite aspect ratio

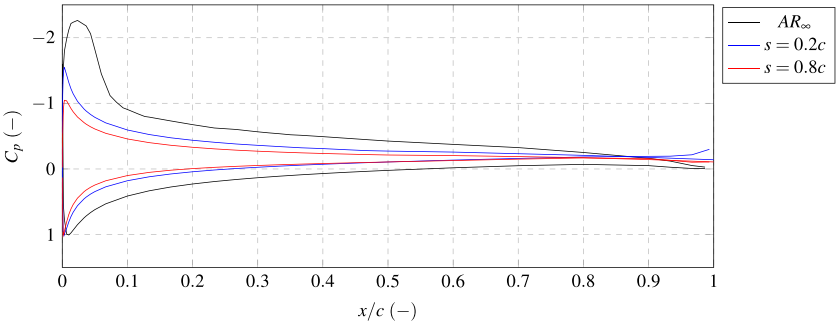

FIG. 27. Comparison of span-wise averaged pressure distribution for the infinite-aspect ratio case with the finite aspect ratio case at two span-wise locations.

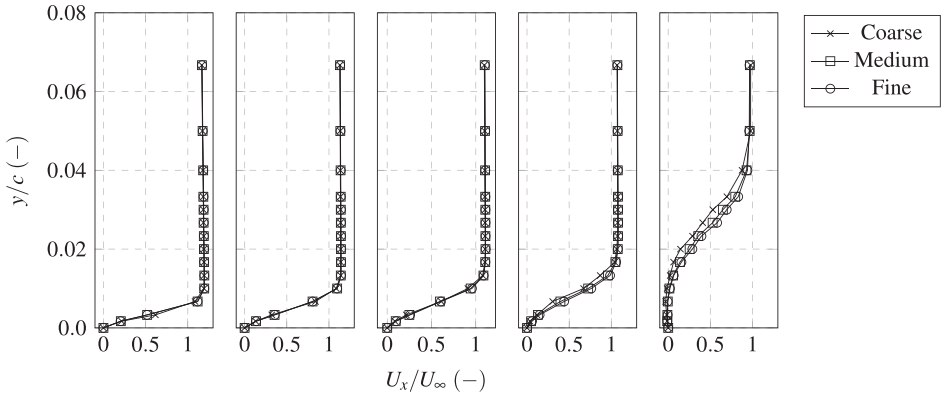

FIG. 28. Mean chord-wise velocity in the boundary layer at $s/c = 0.2$, $x/c = 0.2$, 0.4, 0.6, 0.8, 1.0 for the coarse, medium, and fine meshes at $Re = 1 \times 10^5$ for the finite aspect-ratio wing.

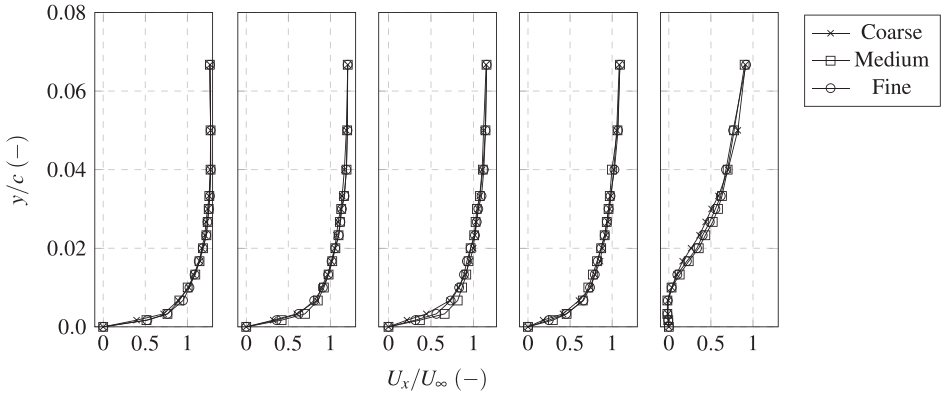

FIG. 29. Mean chord-wise velocity in the boundary layer at $s/c = 0.2$, $x/c = 0.2, 0.4, 0.6, 0.8, 1.0$ for the coarse, medium, and fine meshes at $Re = 1 \times 10^5$ for the infinite aspect-ratio wing.

foils at similar Reynolds numbers and angles of attack, for example, Ref. 56, one would expect the suction-side boundary layer to be more turbulent than it appears to be here.

In Fig. 28, the mean chord-wise velocity in the boundary layer is shown for different chord-wise locations and at a span of $s = 0.2c$. The results are shown for all three grids to demonstrate the grid independence of the data, with excellent agreement seen. For the infinite aspect-ratio case (Fig. 29), the velocity profiles follow a more logarithmic profile which is more consistent with a turbulent boundary layer than is seen for the finite-span case. It can also be seen that the separation close to the trailing edge is more pronounced for the finite aspect-ratio case.

The turbulent nature of the boundary layer for the infinite-span case is revealed by the Q-contours (Fig. 30), which clearly show that the suction-side boundary layer is fully turbulent, with the transition taking place close to the leading edge. Separation at the leading edge leads to transition taking place in the resulting shear layer by way of a Kelvin–Helmholtz mechanism, a process described in detail by Hoarau *et al.*[61] Therefore, the transition takes place here because of the flow separation, which is absent in the finite-span case due to the lower effective angle of attack. This can also be seen in Fig. 31, which shows the instantaneous pressure around the wing for the two cases. As well as the larger pressure differential for the finite-span case, the leading edge separation and transition can also be seen here.

Instead, the growth of a Tollmien–Schlichting wave is observed for the finite-aspect ratio case. This is shown in Fig. 7, with growing chord-wise velocity fluctuations centered around 65 Hz. The boundary layer only becomes fully turbulent at the trailing edge. It is also of interest to consider how the fluctuations change as a function of span. The normalized root mean square of the chord-wise velocity fluctuations is shown in Fig. 32 for different span locations. This shows a decreasing trend moving toward the tip, with the chord-wise fluctuations being highest farthest from the tip. From this, we may infer that the tip affects the boundary layer transition in two ways. First, by preventing leading edge separation, the transition that occurs for the infinite span case is prevented. Second, the T–S instabilities are smaller closer to the tip implying that the tip flow is suppressing the transition by this mechanism as well.

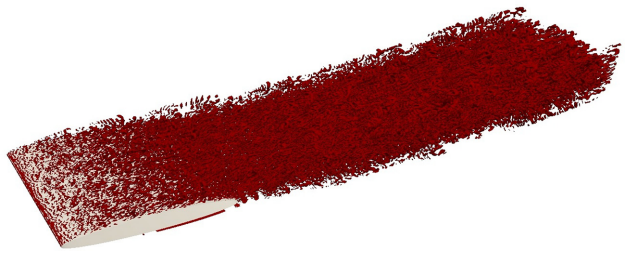

FIG. 30. Normalized iso-Q contours for the infinite aspect-ratio wing at $Re = 1 \times 10^5$.

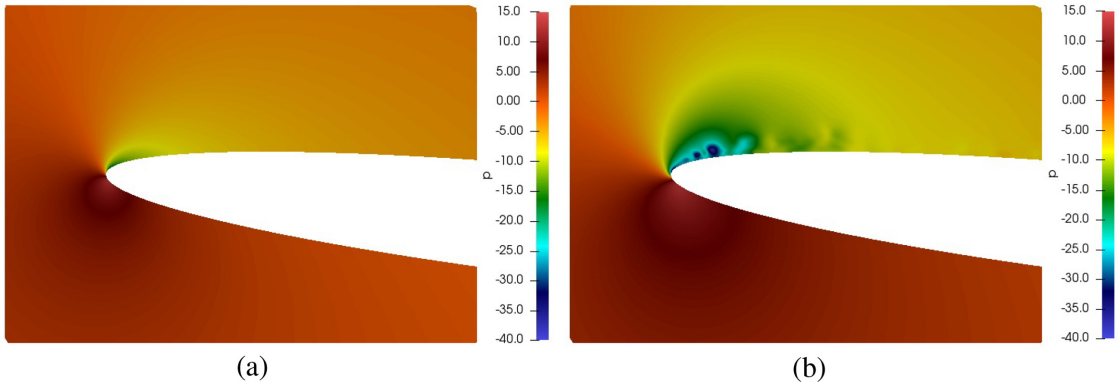

FIG. 31. Instantaneous pressure contours at the leading edge, mid-span for the (a) finite-span and (b) infinite-span cases at $Re = 1 \times 10^5$.

IV. CONCLUSIONS

In this study, DNSs have been conducted to investigate the flow over a finite-aspect ratio elliptical wing at three Reynolds numbers. At each Reynolds number, the simulations have been carried out on three grids in order to assess the level of grid independence with mesh sizes ranging from 12 to 126 million elements. The grid independence has been assessed in several ways, including comparisons of the mean and root mean square forces, boundary layer velocity profiles, as well as first and second-order statistics in the trailing vortex. The excellent agreement seen in the data, particularly for the medium and fine meshes, provides a high level of confidence in the results, allowing for more concrete conclusions to be drawn.

Considerable differences are observed across the range of Reynolds numbers assessed and some clear trends can be drawn from the data. First, there was a core axial velocity deficit across the range and this deficit reduced with increasing Reynolds number. The mean pressure coefficient in the core decreased with increasing Reynolds number, both in the vortices over the tip and in the trailing vortex. Despite these trends, the change in the underlying fluid dynamics has been shown to be highly non-linear as the Reynolds number increases. This makes it difficult to derive quantitative relationships between these parameters and the Reynolds number.

At $Re = 1 \times 10^4$, the vortex roll-up does not take place until downstream of the trailing edge, with the lowest pressure observed at around 1 chord-length downstream. A significant axial velocity deficit is noted, with this being attributed to the vortex forming as a result of fluid wrapping around a region of separated flow at the trailing edge. Higher Reynolds numbers see the emergence of multiple vortical structures over the tip which merge at the trailing edge. Similar mean behavior is noted for the two higher Reynolds numbers in terms of the vortex development and merging. At the highest Reynolds number, the shear layers induced by flow separation over the flat tip are unstable, leading to transition, with turbulent flow becoming entrained in the vortex cores.

For the two higher Reynolds numbers, the multiple vortical structures merge at the trailing edge to form a single turbulent trailing vortex. At the highest Reynolds number, high levels of turbulence in the resulting vortex are shown to originate from unstable shear layers on the pressure and suctions sides of the tip. At $Re = 4 \times 10^4$, the flow has the same mean structure but the shear layers remain stable until close to the trailing edge, where the pressure-side shear layer becomes a source of turbulent kinetic energy.

In the wake, the vortex cores recover both pressure and axial velocity, and the turbulence intensity decays for the two higher Reynolds numbers. For the lowest Reynolds number, the trailing vortex splits into 2 at around 1.5 chord-lengths downstream of the trailing edge. A growing fluctuation originating in the separated flow around which the vortex forms is through to be the reason for this behavior.

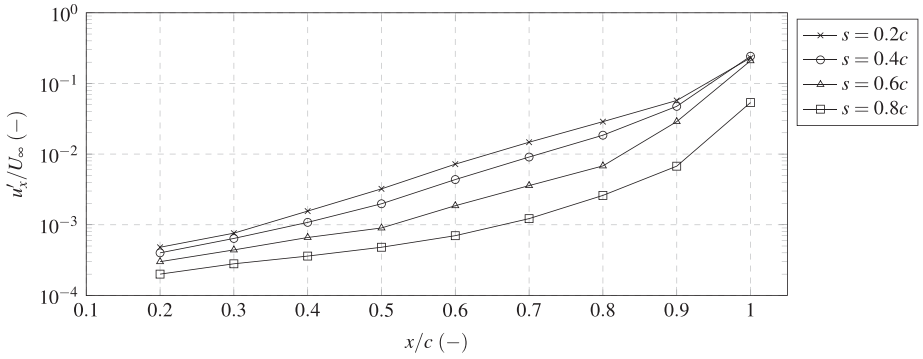

FIG. 32. Root-mean square axial velocity fluctuations in the suction-side boundary layer for the finite-span case at $Re = 1 \times 10^5$.

Finally, a comparison of the highest Reynolds number case with simulations of an infinite-span wing revealed several interesting details relating to the influence of the tip flow on the surface pressure distribution and the boundary layer. As expected, the tip flow reduces the effective angle of attack and so reduces the pressure differential between the pressure and suction sides. This effect is most prominent closest to the tip, but is significant across the entire span. The lower effective angle of attack prevents the leading edge flow separation that is observed for the infinite-span case, preventing the transition of the boundary layer. The suction-side boundary layer instead contains growing Tollmien–Schlichting waves which lead to transition to turbulence at the trailing edge. The wave amplitudes are smaller closer to the tip, indicating that the tip flow acts to reduce this instability.

ACKNOWLEDGMENTS

This research was sponsored by the UK Ministry of Defence and by BMT Defence and Security. The authors also wish to acknowledge the use of the UCL Grace High Performance Computing Facility and associated support services in the completion of this work.

DATA AVAILABILITY

Raw data were generated using the UCL Grace High Performance Computing Facility. Derived data supporting the findings of this study are available from the corresponding author upon reasonable request.

REFERENCES

[1]W. J. Devenport, M. C. Rife, S. I. Liapis, and G. J. Follin, "The structure and development of a wing-tip vortex," J. Fluid Mech. **312**, 67–106 (1996).
[2]B. R. Ramaprian and Y. Zheng, "Measurements in rollup region of the tip vortex from a rectangular wing," AIAA J. **35**, 1837–1843 (1997).
[3]M. Giuni and R. B. Green, "Vortex formation on squared and rounded tip," Aerosp. Sci. Technol. **29**, 191–199 (2013).
[4]P. R. Spalart, "Airplane trailing vortices," Annu. Rev. Fluid Mech. **30**, 107–138 (1998).
[5]L. Jacquin and C. Pantano, "On the persistence of trailing vortices," J. Fluid Mech. **471**, 159–168 (2002).
[6]C. H. K. Williamson, T. Leweke, D. J. Asselin, and D. M. Harris, "Phenomena, dynamics and instabilities of vortex pairs," Fluid Dyn. Res. **46**, 061425 (2014).
[7]D. J. Garmann and M. R. Visbal, "Analysis of tip vortex near-wake evolution for stationary and oscillating wings," AIAA J. **55**, 2686–2702 (2017).
[8]J. R. J. Patterson, "Lift-induced wing-tip vortex attenuation," in 12th Aerospace Science Meeting (1974), p. 38.
[9]R. E. Dunham, Jr., "Unsuccessful concepts for aircraft wake vortex minimization," NASA Report 19780004080, 1977.
[10]T. Lee and Y. Su, "Wingtip vortex control via the use of a reverse half-delta wing," Exp. Fluids **52**, 1593–1609 (2012).
[11]T. Lee and S. Choi, "Wingtip vortex control via tip-mounted half-delta wings of different geometric configurations," J. Fluids Eng. **137**(12), 121105 (2015).
[12]D. Greenblatt, "Fluidic control of a wing tip vortex," AIAA J. **50**, 375–386 (2012).
[13]X. Huang, S. M. A. Moghadam, P. S. Meysonnat, M. Meinke, and W. Schröder, "Numerical analysis of the effect of flaps on the tip vortex of a wind turbine blade," Int. J. Heat Fluid Flow **77**, 336–351 (2019).
[14]J. Keller, P. Kumar, and K. Mahesh, "Examination of propeller sound production using large Eddy simulation," Phys. Rev. Fluids **3**, 064601 (2018).
[15]S. Ianniello, R. Muscari, and A. D. Mascio, "Ship underwater noise assessment by the acoustic analogy. Part I: Nonlinear analysis of a marine propeller in a uniform flow," J. Mar. Sci. Technol. **18**, 547–570 (2013).
[16]S. Ianniello and E. De Bernardis, "Farassat's formulations in marine propeller hydroacoustics," Int. J. Aeroacoust. **14**, 87–103 (2015).
[17]T. van Terwisga, E. van Wijngaarden, J. Bosschers, and G. Kuiper, "Achievements and challenges in cavitation research on ship propellers," Int. Shipbuilding Prog. **54**, 165–187 (2007).
[18]B. W. McCormick, Jr., "On cavitation produced by a vortex trailing from a lifting surface," J. Basic Eng. **84**, 369–378 (1962).
[19]Y. T. Shen, S. Gowing, and S. Jessup, "Tip vortex cavitation inception scaling for high Reynolds number applications," J. Fluids Eng. **131**(7), 071301 (2009).
[20]L. Lignarolo, D. Ragni, F. Scarano, C. S. Ferreira, and G. Van Bussel, "Tip-vortex instability and turbulent mixing in wind-turbine wakes," J. Fluid Mech. **781**, 467–493 (2015).
[21]P. Kumar and K. Mahesh, "Large Eddy simulation of propeller wake instabilities," J. Fluid Mech. **814**, 361–396 (2017).
[22]J. M. Ortega, R. L. Bristol, and Ö. Savaş, "Experimental study of the instability of unequal-strength counter-rotating vortex pairs," J. Fluid Mech. **474**, 35–84 (2003).
[23]R. L. Bristol, J. M. Ortega, P. S. Marcus, and Ö. Savaş, "On cooperative instabilities of parallel vortex pairs," J. Fluid Mech. **517**, 331–358 (2004).
[24]D. Fabre and L. Jacquin, "Viscous instabilities in trailing vortices at large swirl numbers," J. Fluid Mech. **500**, 239–262 (2004).
[25]L. Jiang, J. Cai, and C. Liu, "Large-Eddy simulation of wing tip vortex in the near field," Int. J. Comput. Fluid Dyn. **22**, 289–330 (2008).
[26]J. S. Chow, G. G. Zilliac, and P. Bradshaw, "Mean and turbulence measurements in the near field of a wingtip vortex," AIAA J. **35**, 1561–1567 (1997).
[27]R. F. Huang and C. L. Lin, "Vortex shedding and shear-layer instability of wing at low-Reynolds numbers," AIAA J. **33**, 1398–1403 (1995).
[28]F. G. Irving, *An Introduction to the Longitudinal Static Stability of Low-Speed Aircraft* (Elsevier, 1966).
[29]J. Katz and A. Plotkin, *Low-Speed Aerodynamics*, Vol. 13 (Cambridge university Press, 2001).
[30]K. Zhang, S. Hayostek, M. Amitay, W. He, V. Theofilis, and K. Taira, "On the formation of three-dimensional separated flows over wings under tip effects," J. Fluid Mech. **895**, A9 (2020).
[31]D. J. Moreau and C. J. Doolan, "Tonal noise production from a wall-mounted finite airfoil," J. Sound Vib. **363**, 199–224 (2016).
[32]R. W. Paterson, P. G. Vogt, M. R. Fink, and C. L. Munch, "Vortex noise of isolated airfoils," J. Aircr. **10**, 296–302 (1973).
[33]T. F. Brooks and M. A. Marcolini, "Airfoil tip vortex formation noise," AIAA J. **24**, 246–252 (1986).
[34]O. Fleig, M. Iida, and C. Arakawa, "Wind turbine blade tip flow and noise prediction by large-eddy simulation," J. Sol. Energy Eng. **126**, 1017–1024 (2004).
[35]T. Imamura, S. Enomoto, and K. Yamamoto, "Noise simulation around NACA0012 wingtip using large eddy simulation," Trans. Jpn. Soc. Aeronaut. Space Sci. **55**, 214–221 (2012).
[36]K. B. M. Q. Zaman, A. F. Fagan, and M. R. Mankbadi, "An experimental study and database for tip vortex flow from an airfoil," NASA Report No. 20180000918, 2017.
[37]A. Shekarriz, T. C. Fu, J. Katz, and T. Huang, "Near-field behavior of a tip vortex," AIAA J. **31**, 112–118 (1993).
[38]S. I. Green and A. Acosta, "Unsteady flow in trailing vortices," J. Fluid Mech. **227**, 107–134 (1991).
[39]T. Lee and J. Pereira, "Nature of wakelike and jetlike axial tip vortex flows," J. Aircr. **47**, 1946–1954 (2010).
[40]D. Micallef, C. S. Ferreira, T. Sant, and G. van Bussel, "Experimental and numerical investigation of tip vortex generation and evolution on horizontal axis wind turbines," Wind Energy **19**, 1485–1501 (2016).
[41]J. Dacles-Mariani, G. G. Zilliac, J. S. Chow, and P. Bradshaw, "Numerical/experimental study of a wingtip vortex in the near field," AIAA J. **33**, 1561–1568 (1995).
[42]T. J. Craft, A. V. Gerasimov, B. E. Launder, and C. M. E. Robinson, "A computational study of the near-field generation and decay of wingtip vortices," Int. J. Heat Fluid Flow **27**, 684–695 (2006).
[43]K. Kaufmann, C. C. Wolf, C. B. Merz, and A. D. Gardner, "Numerical investigation of blade-tip-vortex dynamics," CEAS Aeronaut. J. **9**, 373–386 (2018).
[44]J. W. Lombard, D. Moxey, S. J. Sherwin, J. Hoessler, S. Dhandapani, and M. J. Taylor, "Implicit large-Eddy simulation of a wingtip vortex," AIAA J. **54**, 506–518 (2016).

[45]N. Kornev and N. Abbas, "Numerical simulation of the tip vortex behind a wing oscillated with a small amplitude," J. Aircr. **54**, 831–837 (2017).
[46]M. J. Churchfield and G. A. Blaisdell, "Reynolds stress relaxation turbulence modeling applied to a wingtip vortex flow," AIAA J. **51**, 2643–2655 (2013).
[47]R. Muscari, A. D. Mascio, and R. Verzicco, "Modeling of vortex dynamics in the wake of a marine propeller," Comput. Fluids **73**, 65–79 (2013).
[48]A. Uzun, M. Y. Hussaini, and C. L. Streett, "Large-Eddy simulation of a wing tip vortex on overset grids," AIAA J. **44**, 1229–1242 (2006).
[49]A. Uzun and M. Y. Hussaini, "Simulations of vortex formation around a blunt wing tip," AIAA J. **48**, 1221–1234 (2010).
[50]H. Hasebe, Y. Naka, and K. Fukagata, "An attempt for suppression of wing-tip vortex using plasma actuators," J. Fluid Sci. Technol. **6**, 976–988 (2011).
[51]P. Orlandi, G. F. Carnevale, S. K. Lele, K. Shariff, and W. C. Reynolds, "DNS study of stability of trailing vortices," in Centre for Turbulence Research, Proceedings of the Summer Program (1998), pp. 187–208.
[52]M. Abid and M. E. Brachet, "Direct numerical simulations of the batchelor trailing vortex by a spectral method," Phys. Fluids **10**, 469–475 (1998).
[53]H. Shan, L. Jiang, and C. Liu, "Direct numerical simulation of flow separation around a NACA 0012 airfoil," Comput. Fluids **34**, 1096–1114 (2005).
[54]L. E. Jones, R. D. Sandberg, and N. D. Sandham, "Direct numerical simulations of forced and unforced separation bubbles on an airfoil at incidence," J. Fluid Mech. **602**, 175–207 (2008).
[55]M. Gageik, I. Klioutchnikov, and H. Olivier, "Comprehensive mesh study for a direct numerical simulation of the transonic flow at Rec = 500,000 around a NACA 0012 airfoil," Comput. Fluids **122**, 153–164 (2015).
[56]T. A. Smith and Y. Ventikos, "Boundary layer transition over a foil using direct numerical simulation and large Eddy simulation," Phys. Fluids **31**, 124102 (2019).
[57]R. I. Issa, "Solution of the implicitly discretised fluid flow equations by operator-splitting," J. Comput. Phys. **62**, 40–65 (1986).
[58]D. Mavriplis and V. Venkatakrishnan, "A 3D agglomeration multigrid solver for the Reynolds–averaged Navier–Stokes equations on unstructured meshes," Int. J. Numer. Methods Fluids **23**, 527–544 (1996).
[59]J. C. R. Hunt, A. A. Wray, and P. Moin, "Eddies, streams, and convergence zones in turbulent flows," (Centre for Turbulence Research, 1988).
[60]A. Nicolle and I. Eames, "Numerical study of flow through and around a circular array of cylinders," J. Fluid Mech. **679**, 1–31 (2011).
[61]Y. Hoarau, M. Braza, Y. Ventikos, D. Faghani, and G. Tzabiras, "Organized modes and the three-dimensional transition to turbulence in the incompressible flow around a NACA0012 wing," J. Fluid Mech. **496**, 63–72 (2003).